

Lateral Thermo-magneto-optoelectronic Effects in a 3C-SiC Nanothin Film on the Si Heterojunction

Dinh Gia Ninh,* Tuan-Hung Nguyen, Cong Thanh Nguyen, Nguyen Vu Thu Hien, Dang D.H. Tran, Pablo Guzman, Braiden Tong, Hong-Quan Nguyen, Emily Lakis, Trung-Hieu Vu, Erik W. Streed, Yong Zhu, Tuan-Khoa Nguyen, Van Thanh Dau, Nam-Trung Nguyen, and Dzung Viet Dao*



Cite This: *J. Phys. Chem. C* 2024, 128, 1284–1297



Read Online

ACCESS |



Metrics & More

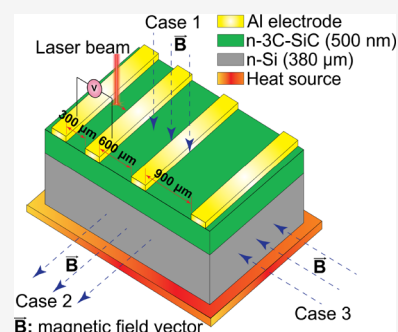


Article Recommendations



Supporting Information

ABSTRACT: The lateral photovoltaic effect (LPE) of an n-type cubic silicon carbide (n-3C-SiC) on an n-type silicon (n-Si) heterostructure in a thermo-magnetic environment is examined for the first time in this study for use in position-sensitive detectors (PSDs). Under 2 mW of 637 nm laser irradiation and at room temperature ($T = 298$ K), the n-3C-SiC/n-Si device with an electrode spacing of $300 \mu\text{m}$ demonstrated an excellent position sensitivity of 442 mV/mm . The study shows that the thermal and magnetic fields have significantly affected the sensitivity of the PSD device. In addition, this research presents the photogeneration and transportation of electron–hole pairs in the heterostructure under the influence of heat and magnetic field in three directions of the Cartesian coordinate system. The underpinning physic mechanism of charge carrier movement in the heterojunctions as well as the generation and separation of electron–hole pairs in a self-power mode is employed to explain physical phenomena in the paper. The findings will have a significant impact on the development of PSDs that not only function under challenging conditions but also demonstrate the potential of magnetic and thermal sensors. This opens up a promising signal for thermal and magnetic sensors with a self-power mode that draws power from natural light (sunlight).



1. INTRODUCTION

As the globe faces the difficulties of energy depletion, environmental degradation, and unprecedented climate change, the creation of green energy utilizing natural light has emerged as a hot research topic in science and technology. The conversion of natural light energy into other types of energy requires strong support from the semiconductor and microelectronics industries. In the modern era of IoT technology, electronic and sensing devices play a vital role in artificial intelligence,^{1–5} smart industries and robotics,^{6–10} and medical applications^{11–15}; thus, enhanced sensing effects have attracted the interest of scientists and researchers. Self-powered optoelectronic devices are emerging as one of the important applications of the micro/nano technology industry, with excellent applications including photodetectors,^{16–20} energy harvesters,^{21–24} position sensitive detectors,^{25–28} and solar cells.^{29–32}

The position-sensitive detector (PSD) is one of the most important types of noncontact position sensors, and it has many practical applications in angle measurement, high-speed trajectory tracking, and vibration frequency measurement. The lateral photovoltaic effect (LPE) has been extensively applied to developing PSDs and relies on the linear relationship between the lateral photovoltage and laser spot position between two electrodes. Ma et al.³³ investigated the optoelectronic behaviors and self-powered operation of a

PSD using the $\text{Ag}_2\text{Se}/\text{p-Si}$ heterostructure based on LPE. The sensitivity of this structure was 2.8 mV/mm under 1064 nm NIR illumination without any applied bias voltage. The coupled photovoltaic–pyroelectric effect improved the transient lateral photovoltage (LPV) response with a maximum enhancement of 1797% under NIR illumination through variation of the chopper frequency. Another heterostructure based on the combination of Ag nanoparticle-embedded silk protein ($\text{Ag}/\text{silk protein}/\text{Si}$) was reported by Cao et al.³⁴ The maximum sensitivity was 308.3 mV/mm , which was considered a high sensitivity value in organic materials. Cong et al.³⁵ studied the characteristics of a PSD fabricated using vertically oriented layered MoS_2/Si nanosheets. The device achieved excellent lateral photovoltaic performance in a wide range of wavelengths ranging from visible to near-infrared light. Ultrahigh position sensitivity over a wide spectrum ranging from 350 to 1100 nm was measured up to 401.1 mV/mm . In addition, an ultrafast response of 16 ns under highly stable conditions and excellent reproducibility were obtained. The

Received: September 13, 2023

Revised: November 11, 2023

Accepted: November 14, 2023

Published: December 1, 2023



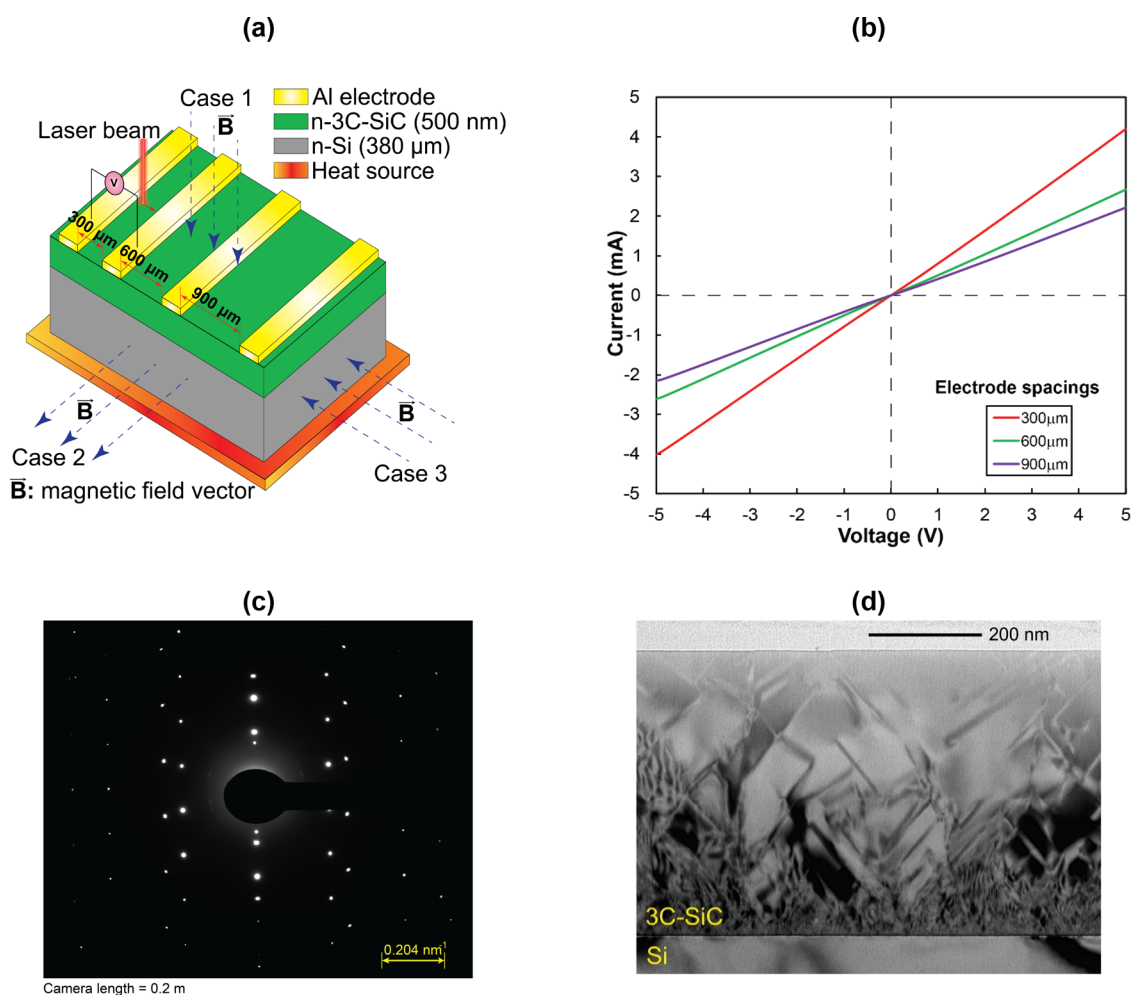


Figure 1. Designed structure and material characterizations. (a) The n-3C-SiC/n-Si heterostructure with three different electrode spacings. (b) Current–voltage characteristics in dark conditions. (c) SAED image of the 3C-SiC nano thin film. (d) Cross-sectional TEM image of 3C-SiC on the Si substrate.

experiments indicated that the intralayer time was 5 ns and the interlayer transport time was 11 ns in V-MoS₂. Wang et al.³⁶ reported a sensitivity of 32.5 mV/mm in a Fe₃O₄/Si Schottky junction PSD with a fast response relaxation time in the order of microseconds. The defect-promoted photothermoelectric effect in a densely aligned ZnO nanorod array for self-powered position detection was investigated by Du et al.³⁷ In this study, a defect-rich ZnO device with high electrical conductivity and a large Seebeck coefficient was found to improve the photothermoelectric energy conversion and position sensitivity significantly. Position sensitivity was 0.19 mV/mm, and the temperature-gradient-induced electric field compensated for suppression in the photothermoelectric process. A heterostructure using hybrid organic/inorganic PSDs based on poly(3,4-ethylenedioxythio-phenylene) polystyrenesulfonate/n-Si was implemented by Javadi et al.³⁸ The sensitivity was recorded over 100 mV/mm with an excellent nonlinearity of below 3%, whereas the response correlation coefficient was over 0.995 with a response time of less than 4 ms under inhomogeneous IR illumination. Many other heterostructures are used to develop photodetectors and PSDs, such as graphene/SiO₂/Si,³⁹ Si/In₂Se₃,⁴⁰ different nanostructured ZnO,⁴¹ Ni/p-Si,⁴² ZnO/Si,⁴³ SnSe/SiO₂/Si,⁴⁴ hybrid perovskite (organic–inorganic halide perovskite),^{45,46} glass/Mo/

CIGS/CdS/ZnO/ITO structure,⁴⁷ and Au/MgO/MgZnO metal oxide semiconductor.⁴⁸

The impact of the magnetic field on nonmagnetic materials is an intriguing and essential study issue in materials science and physics. Although nonmagnetic materials do not contain magnetic moments, they can display a range of magnetic field effects that have profound consequences for their characteristics and uses. Magnetoresistance is a well-known example of the magnetic field effect on nonmagnetic materials in which the electrical resistance of a material varies in reaction to the application of a magnetic field. This phenomenon has crucial practical implications in disciplines such as magnetic data storage and magnetic sensing, and it has been widely studied in a broad range of materials, including metals, semiconductors, and even organic materials.^{49–52} In this study, we introduce a nonmagnetic material 3C-SiC/Si heterostructure to investigate the effect of the magnetic field and temperature on optoelectronic properties of this structure. SiC is known for its excellent robust mechanical, electrical, and chemical properties and is used for high-power electronics and MEMS/NEMS devices for harsh environments.^{53–57} 3C-SiC is one of the polytypes of SiC that can be grown directly on widely available silicon substrates to form a 3C-SiC/Si heterojunction. 3C-SiC itself has many advantages, such as a wide energy bandgap of around 2.38 eV and the ability to work

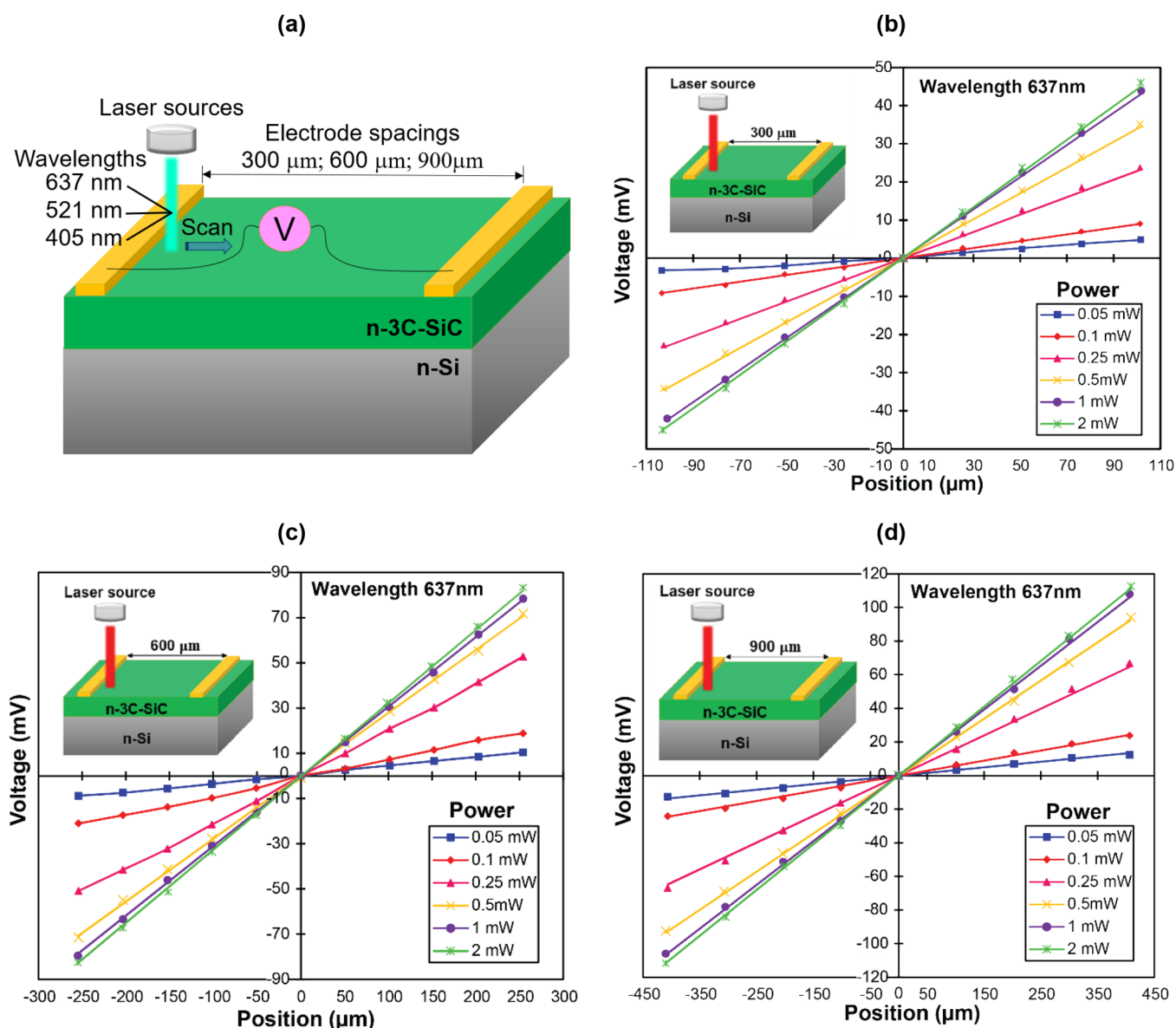


Figure 2. Effects of electrode spacings and wavelength on a position-sensitive detector at room temperature and without a magnetic field. (a) Configuration of the n-3C-SiC/n-Si heterostructure with various wavelengths and electrode spacings. (b–d) The LPV–position relationships measured on electrode spacings of 300, 600, and 900 μm , respectively, under wavelengths of 637 nm.

in high-temperature, chemically corrosive, and high-pressure environments. Thanks to the advanced microfabrication process and the outstanding electronic properties of Si and SiC, the 3C-SiC/Si heterojunction holds great promise for the development of optoelectronic devices. However, the potential of 3C-SiC/Si as a PSD has not been fully explored, especially in the context of working in complicated environments. The n-3C-SiC/n-Si heterostructure, which has a self-powered mode fueled by sunlight, is expected to have potential applications in various domains such as sensing applications (thermal sensors, optical sensors, and magnetic sensors), energy harvesting, and micro/nano electromechanical systems.

We examine the lateral thermo-magneto-optoelectronic effects in this research using the n-type-3C-SiC heterostructure with bandgap (2.38 eV) and n-type Si with bandgap (1.12 eV) for several reasons. First, to the best of the authors' knowledge, no previous research on the n-3C-SiC/n-Si heterostructure has been conducted, particularly under complicated conditions

such as temperature and magnetic fields. Second, the degree of the sensor effects in question is determined by the product of electron mobility and magnetic induction; thus, the n-type semiconductor material is preferable than the p-type material due to the significantly higher electron mobility.⁵⁸ A small bandgap is a disadvantage due to the intrinsic behavior prevailing at room temperature⁵⁸; thus, the wide bandgap is also an advantage of 3C-SiC. In addition, n-3C-SiC/n-Si in the complex environment of temperature and magnetic field is a very practical and popular problem. Therefore, the characteristics of a self-powered n-3C-SiC/n-Si PSD subjected to thermo-magnetic effects are presented. LPE was studied in n-3C-SiC/n-Si heterostructure devices with three different electrode spacings (300, 600, and 900 μm) using a focused laser beam as the nonuniform illumination source. Excellent position sensitivity at zero-bias conditions was measured at 442 mV/mm in the electrode spacing 300 μm under 637 nm wavelength and 2 mW power at room temperature ($T = 298$

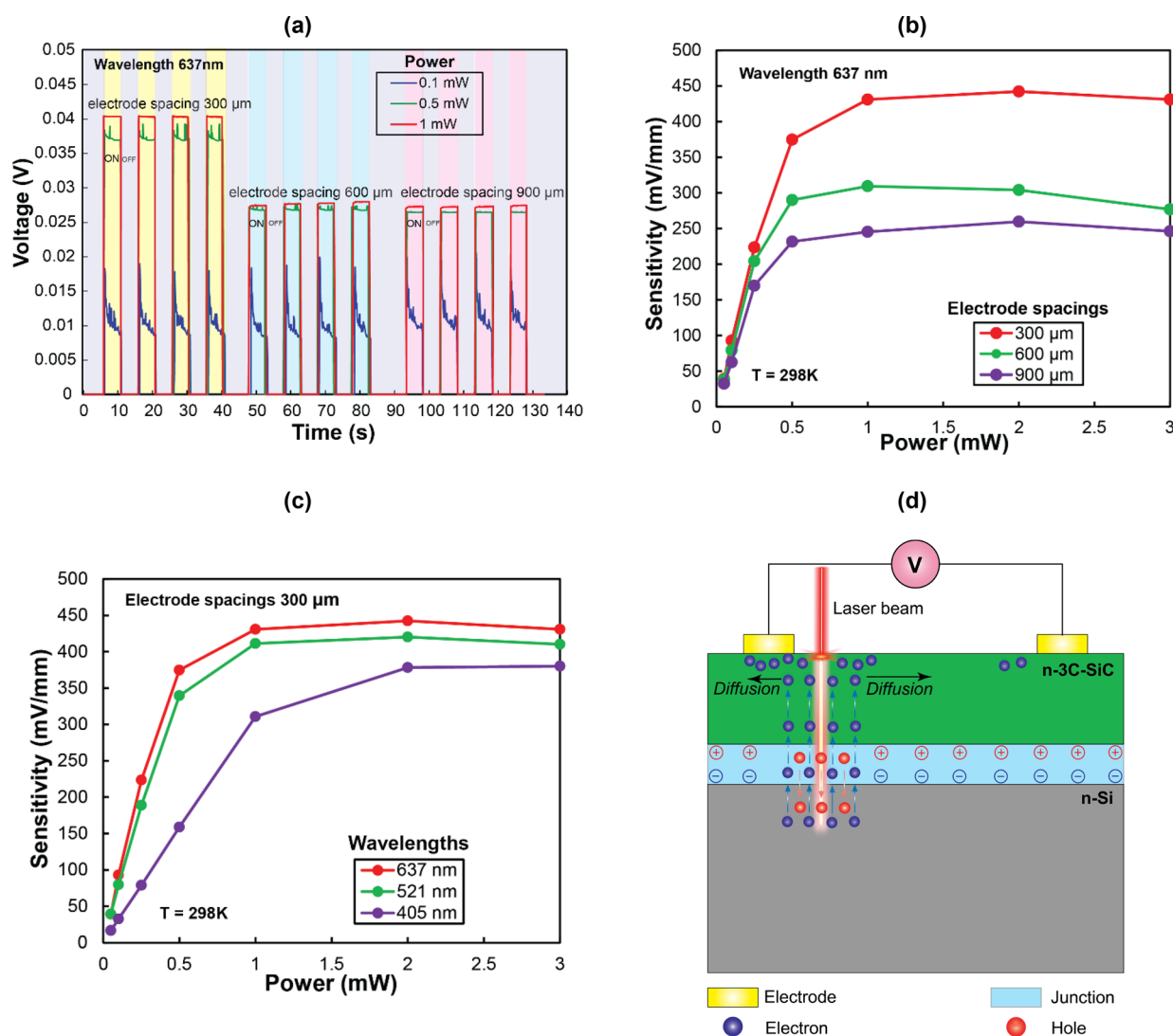


Figure 3. Characterizations of electrical and optoelectronic properties of an n-3C-SiC/n-Si heterostructure at room temperature. (a) Repeatability of LPV at different lighting powers (0.1, 0.5, and 1 mW) for three electrode spacings (300, 600, and 900 μm). (b) Sensitivity–power relationship for three electrode spacings and wavelength of 637 nm. (c) Sensitivity–power relationship for three different wavelengths and electrode spacing of 300 μm . (d) Carrier generation and transportation under illumination conditions.

K). The LPV and the sensitivities of the device were significantly influenced under the concurrent influence of both temperatures and a magnetic field. The experiments were conducted at different electrode spacings, illumination powers, temperatures, and magnetic field directions. Photoexcitation, generation and separation, and transportation of electron–hole (e–h) pairs are used to explain experimental results when the devices are operating in complex environments. It is anticipated that this study can unlock the potential of n-3C-SiC/n-Si heterostructures for applications in optoelectronic field while concurrently showing the significant impact of complex environmental factors, such as thermo-magneto-optical conditions, on the practical performance of these devices.

2. METHODOLOGY AND EXPERIMENT

2.1. Materials and Device Fabrication. To investigate the optoelectronic effects of the heterostructure under the opto-thermo-magnetic conditions, 3C-SiC/Si heterostructure

devices with different electrode spacings (300, 600, and 900 μm) were designed as shown in Figure 1a.

Figure S1 (Supporting Information) shows the fabrication process of the 3C-SiC/Si heterostructure devices. In this process, a 500 nm single crystalline 3C-SiC (100) thin film was grown epitaxially on a 380 μm -thick Si (100) substrate by low-pressure chemical vapor deposition (LPCVD) at 1000 $^{\circ}\text{C}$ employing propylene and silane as precursors. The 3C-SiC film was unintentionally doped using nitrogen (N) in the atmosphere.⁴² The carrier concentrations of the n-doped SiC film and Si substrate were around 3×10^{17} and 8×10^{14} cm^{-3} , respectively. An aluminum layer was patterned on the 3C-SiC film by sputtering and a photolithography process (i.e., photoresist spin-coating, mask alignment, and UV light exposure), which was followed by wet chemical etching of Al. The desired samples were finally diced from the wafer. Figure 1b shows the current–voltage (I – V) relationship of the heterostructure device. The highly linear relationship indicates that the Al electrodes formed good Ohmic contacts with the 3C-SiC surface. Furthermore, at the same voltage, the larger the electrode spacing is, the smaller is the current because of

the higher resistance. The selected area electron diffraction (SAED) in Figure 1c shows that the grown 3C-SiC nanofilm is single-crystalline with a cubic structure. The high-resolution image of transmission electron microscopy (TEM) describes that the grown 3C-SiC is crystallized with the Si very well in Figure 1d.

2.2. Experimental Setup. Figure S2 shows the experimental setup used to characterize the LPE on an n-3C-SiC/n-Si heterostructure in different thermal and magnetic field environments. The light source was placed on a three-axis micropositioning device (Mitutoyo), which can move precisely on three axes of XYZ space. To investigate the LPE and sensitivity of the 3C-SiC/Si PSD, the laser beam was perpendicular to the top surface of the 3C-SiC layer. Laser sources (Thorlabs) with different wavelengths 405, 521, and 635 nm were used in this experiment, and the diameter of the laser spot was 100 μm . The position of the laser spot on the sample was carefully monitored on a computer using a digital microscope (MV30801-WNC, Microvue), and the laser spot diameter was monitored by a beam profiler (BC106N-VIS, Thorlabs). To measure the LPV and the position sensitivity of the heterostructure at various temperatures, the sample was mounted on a Linkam temperature stage (HFS600EPB4) controlled by a temperature controller (T95). The surface temperature of the device was measured using a thermocouple (METEX, M-6000H). The electrical characteristics of the 3C-SiC/Si heterostructure were measured by a Keithley 2450 SourceMeter. The light source power was measured by a power meter (PM100D, Thorlabs) and a power sensor (S130C, Thorlabs). The experiments were performed in a dark room within the standard ambient conditions. Photographs of the experimental instruments and setup are provided in Figure S3.

3. RESULTS AND DISCUSSION

Figure 2a shows the configuration of the n-3C-SiC/n-Si heterostructure (with three electrode spacings of 300, 600, and 900 μm) used for measuring the LPV with three different wavelengths of 637, 521, and 405 nm. Figure 2b–d depicts the linear relationship between the generated LPV and the laser position at a wavelength of 637 nm, whereas Figure S4 shows this relationship at wavelengths of 521 and 405 nm, across a spectrum of illumination powers ranging from 0.05 to 2 mW. The linear relationship demonstrates the potential of the heterostructure for position sensing. It is observed that the LPVs are largest for the red wavelength (637 nm) and smallest for the purple wavelength (405 nm). This is because longer wavelengths are typically absorbed better and provide higher photon conversion efficiency in Si. In addition, during the laser beam scanning process from electrode A to B (electrode spacing 300 μm), from electrode B to C (electrode spacing 600 μm), and from electrode C to D (electrode spacing 900 μm), the maximum LPV value occurs when the laser is in close proximity to the electrodes, whereas the LPV value becomes zero when the laser is positioned at the center. The graphs illustrate that, for a given position from the center between two electrodes, the LPV of the 300 μm electrode spacing exhibits the highest value, gradually decreasing as the electrode spacing is increased. This trend is entirely justifiable because of the migration of numerous electrons toward the 3C-SiC layer at the location where the laser spot is applied. Notably, closer proximity to the electrode results in a higher photovoltage. A

more comprehensive explanation of this phenomenon is provided in the subsequent section.

Figure 3a shows the photoresponse of the device when the laser light is turned on and off periodically at three powers (0.1, 0.5, and 1 mW). We measure the photoresponse when the laser is 76 μm from the central position between the two electrodes. The response and recovery times of the n-3C-SiC/n-Si heterostructure with three electrode spacings (300, 600, and 900 μm) are shown in Table S1 of the Supporting Information. When the laser power is increased, there is a corresponding increase in the LPV. We observed that the heterostructure with a 300 μm electrode spacing exhibits the highest LPV. This finding suggests that, without other external power sources, the LPV generated under nonillumination conditions possesses the potential to function as a self-powered sensor. Furthermore, it is noteworthy that the device has good repeatability across various light power levels. In Figure 3b, the sensitivity–power relationships of the heterostructure with different electrode spacings are shown, whereas Figure 3c presents the sensitivity–power relationship of the heterostructure under three different laser wavelengths. As shown in Figure 3b, when illuminated by a laser with a 637 nm wavelength, the highest sensitivity is observed at 442 mV/mm (with a 2 mW laser power) for an electrode spacing of 300 μm . For the 600 μm electrode spacing, the sensitivity reaches a peak of approximately 300 mV/mm at 1 mW, gradually declining at 2 mW and further at 3 mW. The highest sensitivity in the 900 μm electrode spacing is approximately 250 mV/mm. Interestingly, when the distance between the two electrodes remains constant (as shown in Figure 3c), a longer wavelength corresponds to greater positional sensitivity. Specifically, the sensitivities of the n-3C-SiC/n-Si heterostructures peak at 442, 411, and 378 mV/mm at red (637 nm), green (521 nm), and purple (405 nm) wavelengths, respectively.

The generation and diffusion mechanisms of charge carriers under nonuniform illumination are illustrated in Figure 3d. A junction is created between n-3C-SiC and n-Si when they come into contact. Because the heavily doped 3C-SiC layer is n-type, many electrons here tend to diffuse to the n-Si layer, creating positive charges (red symbols) at the junction. Similarly, holes in the n-Si layer diffuse onto the n-3C-SiC layer, leaving behind negative charges (blue symbols) at the junction. This creates a depletion region and a built-in-electric field formed at the junction of the n-3C-SiC/n-Si heterostructure. When the device is illuminated, because of the thin n-3C-SiC layer, light passes through the SiC layer and is absorbed mainly in the Si layer as well as the junction region. The laser light excites the electrons from the valence band to the conduction band, leaving behind holes in the valence band. This creates electron–hole (e–h) pairs, and under the action of an electric field, these e–h pairs are separated; that is, the electrons migrate toward the SiC layer, whereas the holes move toward the Si layer. Assuming that the laser light is positioned in close proximity to electrode A, the concentration of charge carriers near this electrode will be higher than at electrode B. This charge carrier gradient induces the diffusion of generated charge carriers toward electrode B, as illustrated in Figure 3d. The difference in charge carriers between the two electrodes results in the generation of a voltage across electrodes A and B, referred to as the LPV. The magnitude value of this LPV depends on the laser position. The density of

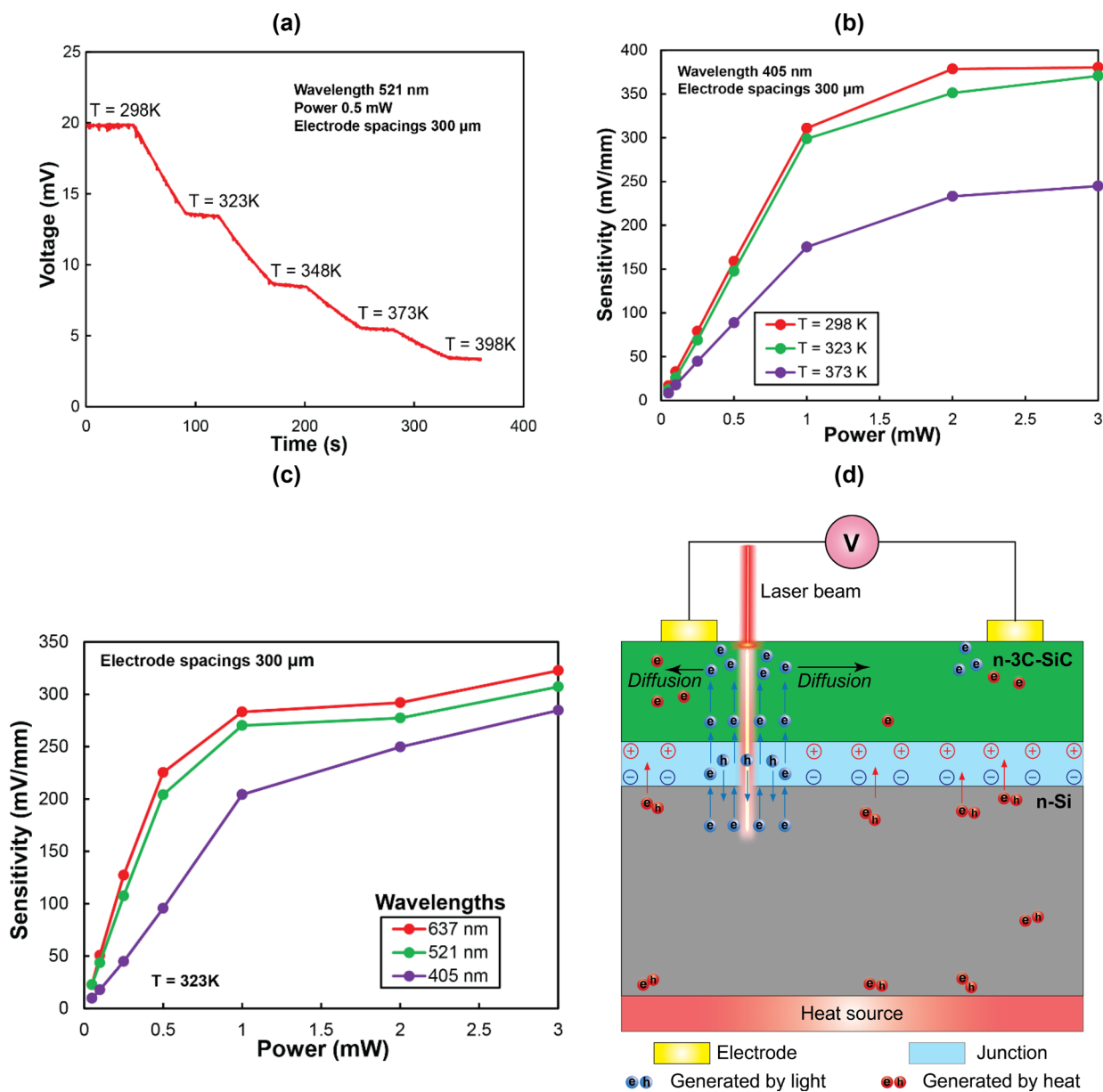


Figure 4. Effect of temperature on device characterizations at electrode spacing of 300 μm. (a) LPV of increasing temperature at the wavelength 521 nm. (b) Sensitivities of devices at different temperatures (298, 323, and 373 K) with wavelength of 405 nm. (c) Sensitivity–power relationship of devices at three wavelengths at a temperature of 323 K. (d) Charge carrier generation and transportation mechanism under illumination and heating conditions.

the electron is defined by the absorption theory⁵⁹ as $n(\nu)$ (ν : the laser frequency):

$$n(\nu) = K_1(h\nu - E_g)^\alpha \quad (1)$$

in which E_g is the energy bandgap of Si, K_1 is a proportional coefficient, and α is an exponential coefficient.

Each electron among $n(\nu)$ can be re-excited statistically [$\tau p/n(\nu)$] times on average (τ is a time related coefficient).⁶⁰ The photogenerated e–h pairs are separated by the built-in electric field that sweeps the electrons toward the SiC layer, whereas the holes move toward the Si substrate. The injected electrons concentration at the SiC can be written as⁶⁰

$$N(\nu) = n(\nu)[1 - P_1^{\tau p/n(\nu)}] \quad (2)$$

where P_1 is the possibility that the electrons recombine with holes and p is the laser power.

The LPV between two electrodes (V_{AB}) and the sensitivity of the PSD (Se) are calculated^{26,28,61,62} as follows:

$$V_{AB} = \frac{2R_2N(\nu)}{d} e^{(-L/d)x} \quad (3)$$

$$Se = \frac{2R_2N(\nu)}{d} e^{(-L/d)} \quad (4)$$

where R_2 is a proportional coefficient and depends on Fermi levels, x is the laser position, $2L$ is the distance between two electrodes, and d is the diffusion length of electrons in SiC.

If the laser illumination is precisely at the center between the two electrodes, the LPV will be zero, as the diffusion of charge carriers occurs symmetrically. This symmetry results in the

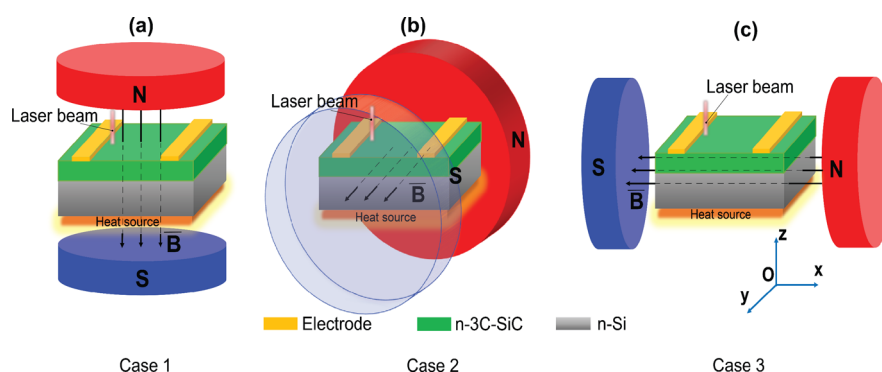


Figure 5. Setups to investigate the LPE of the n-3C-SiC/n-Si heterostructure under different opto-thermo-magnetic effects for electrode spacing 300 μm . (a) The magnetic field vector \vec{B} is oriented in the opposite direction to the Oz axis. (b) The magnetic field vector \vec{B} aligns in the same direction as the Oy axis. (c) the magnetic field vector \vec{B} is oriented in the opposite direction to the Ox axis.

absence of a charge carrier gradient between the two electrodes, and consequently, there is no voltage between the two electrodes.

Figure 4 displays the thermo-optoelectronic characteristics of the n-3C-SiC/n-Si heterojunction. In Figure 4a, we observe a reduction in the LPV as the temperature is elevated from 298 to 398 K. The laser position is 76 μm from the central position between the two electrodes, and the laser power is set at 0.5 mW, at a wavelength of 521 nm. Notably, when the temperature increases from 298 to 323 K, there is a significant decrease of 31.1% in LPV, and this trend continues as the temperature rises further. The LPV decreases by 38% when the temperature rises from 373 to 398 K. Figure 4b depicts the device's position sensitivity versus laser power at the wavelength of 405 nm and at different temperatures. It is observed that the sensitivity decreases as the temperature increases to 323 and 373 K. It is worth noting that there is a sharp 34% sensitivity drop at 3 mW power when the temperature increases from 323 to 373 K. Figure 4c displays the sensitivity of the n-3C-SiC/n-Si heterostructure at three different wavelengths, all measured at a temperature of 323 K. In comparison with the results shown in Figure 3d, we observe that the device's sensitivity in Figure 4c experienced a reduction of up to 25% as the temperature increased from room temperature (298 K) to 323 K. In addition, the sensitivity demonstrates a rapid increase from a light power of 0.05 to 1 mW followed by a more gradual increase from 1 to 3 mW. To provide a clearer explanation for this behavior, Figure 4d illustrates the movement of electron–hole pairs (e–h pairs) within the heterostructure when subjected to the simultaneous influence of light and temperature. Under the effect of heat, charge carriers in the Si substrate become thermally activated and move in a random, chaotic manner. More charge carriers in the Si substrate are excited by heat when the temperature is increased. The charge carrier generated by the light has a smaller quantity, as shown in Figure 4d. The carrier concentration is temperature-dependent and is expressed as follows⁶³:

$$c = T^{(3/2)} e^{(-E_a/k_B T)} \quad (5)$$

where E_a is the activation energy of dopants (phosphorus in the case of n-Si and nitrogen in the case of n-3C-SiC), k_B is the Boltzmann constant, and T is temperature.

At higher temperatures, the temperature-generated e–h pairs are more dominant than the light-generated e–h pairs. Owing to the built-in electric field across the heterojunction,

electrons are attracted and move toward the n-3C-SiC layer. Here, the difference in electron concentrations between the two electrodes is not substantial, resulting in reduction of both the LPV and the sensitivity of the device. Furthermore, the LPV influenced by temperature is also described by $V_{AB} \sim \frac{k_B}{dT^{1/2}} e^{(E_a/k_B T)}$ ⁶⁴; it is evident that with an increase in the temperature, the LPV decreases.

If the heat source is uniformly applied to the entire backside of the Si substrate and the device is not illuminated, the electron–hole pairs will be generated by the thermal energy, and they will move randomly in all directions in the Si substrate. In the presence of a built-in electric field at the heterojunction, electrons will migrate toward the 3C-SiC layer and move toward the electrodes. Because the heat generation is uniform, the charge carriers (mainly electrons) will also distribute uniformly/equally between the two electrodes, resulting in a zero voltage difference between the two electrodes.

If the heat source is applied asymmetrically near one electrode and the device is not illuminated, electron–hole pairs will be generated by the thermal energy. Electrons will migrate toward the 3C-SiC layer and accumulate more at the electrode that is heated. Meanwhile, the other electrode will receive much less electrons. This difference in the electron density between the two electrodes will result in a lateral voltage between the two electrodes.

In the next section, the thermo-magneto-optoelectronic characteristics of the n-3C-SiC/n-Si heterojunction device are investigated with three different cases of magnetic field \vec{B} , as shown in Figure 5. The output voltage is measured between two electrodes on the 3C-SiC surface. Next, we will analyze the results, explaining the underpinning physics behind each case.

1. Case 1

Figure 5a shows the setup to investigate the LPE of the n-3C-SiC/n-Si heterostructure under different opto-thermo-magnetic effects for electrode spacing of 300 μm . The relationship between device sensitivity and laser power at a temperature of 323 K and magnetic field of 0.46 T is shown in Figure 6a. Notably, the relationship appears highly linear across all three wavelengths tested, and the device does not exhibit saturation even when the laser power is increased to 3 mW. Moreover, it is worth highlighting that when subjected to heat and magnetic fields, the sensitivity of the device at each laser power level is considerably lower

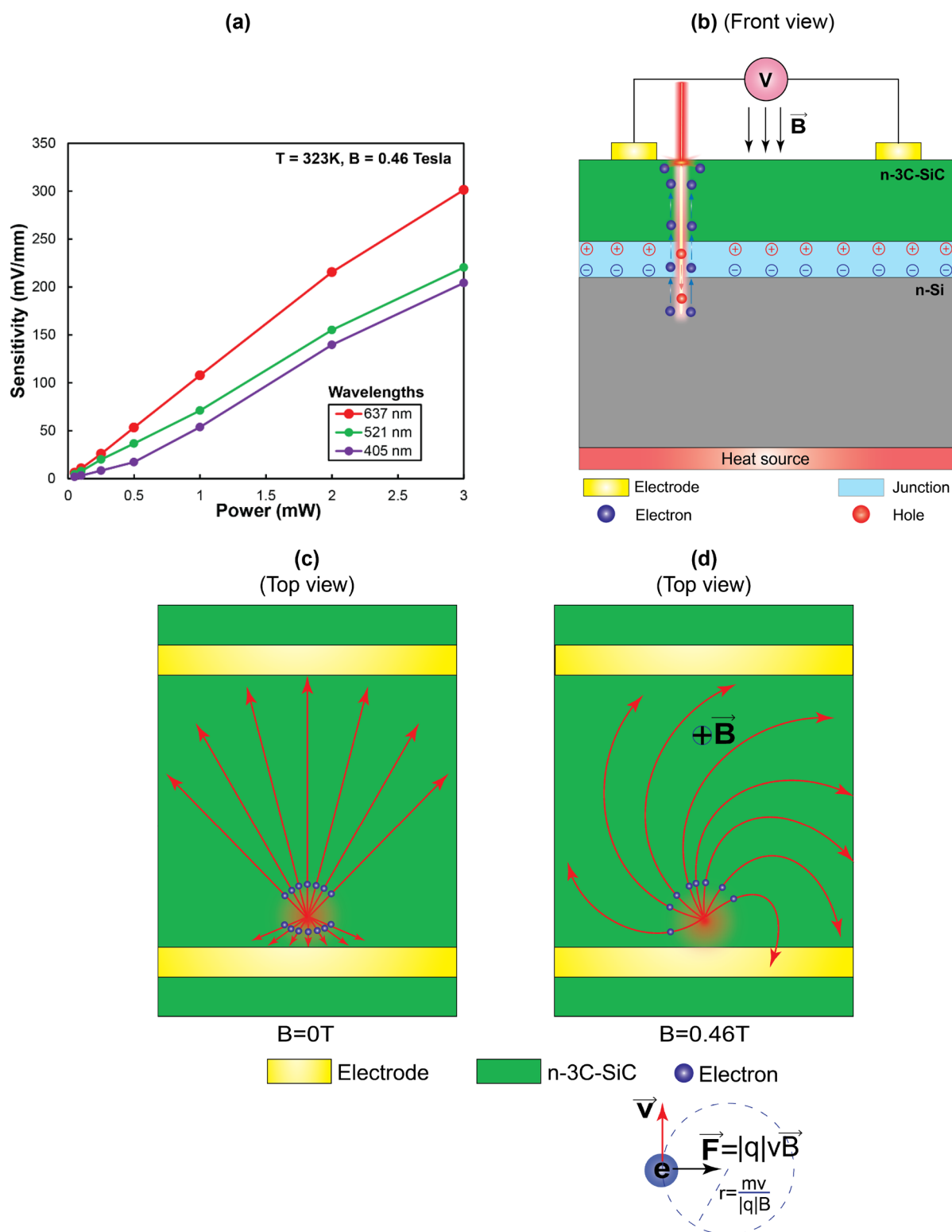


Figure 6. Impact of opto-thermo-magnetic effects on the n-3C-SiC/n-Si heterojunction in case 1. (a) Sensitivity–power relationship at three wavelengths under thermo-magneto impacts (temperature is 323 K, and the magnetic field is 0.46 T). (b) Charge carrier generation and transportation mechanism under thermal and light impacts. (c) The diffusion current distribution in the n-3C-SiC layer without magnetic field and the direction of movement of electrons. (d) The diffusion current distribution in the n-3C-SiC layer with magnetic field and the direction of movement of electrons.

than when it is exposed solely to opto-thermo effects. This can be explained in Figure 6b–d. Under the effect of laser light and heat, e–h pairs are generated and split due to the built-in electric field. Electrons tend to move

to the n-3C-SiC layer (explained in Figure 3d). When the whole device is placed in a magnetic field \vec{B} as shown in Figure 5a, the Lorentz force acts on the moving charged particles. Specifically, in the Si substrate, the

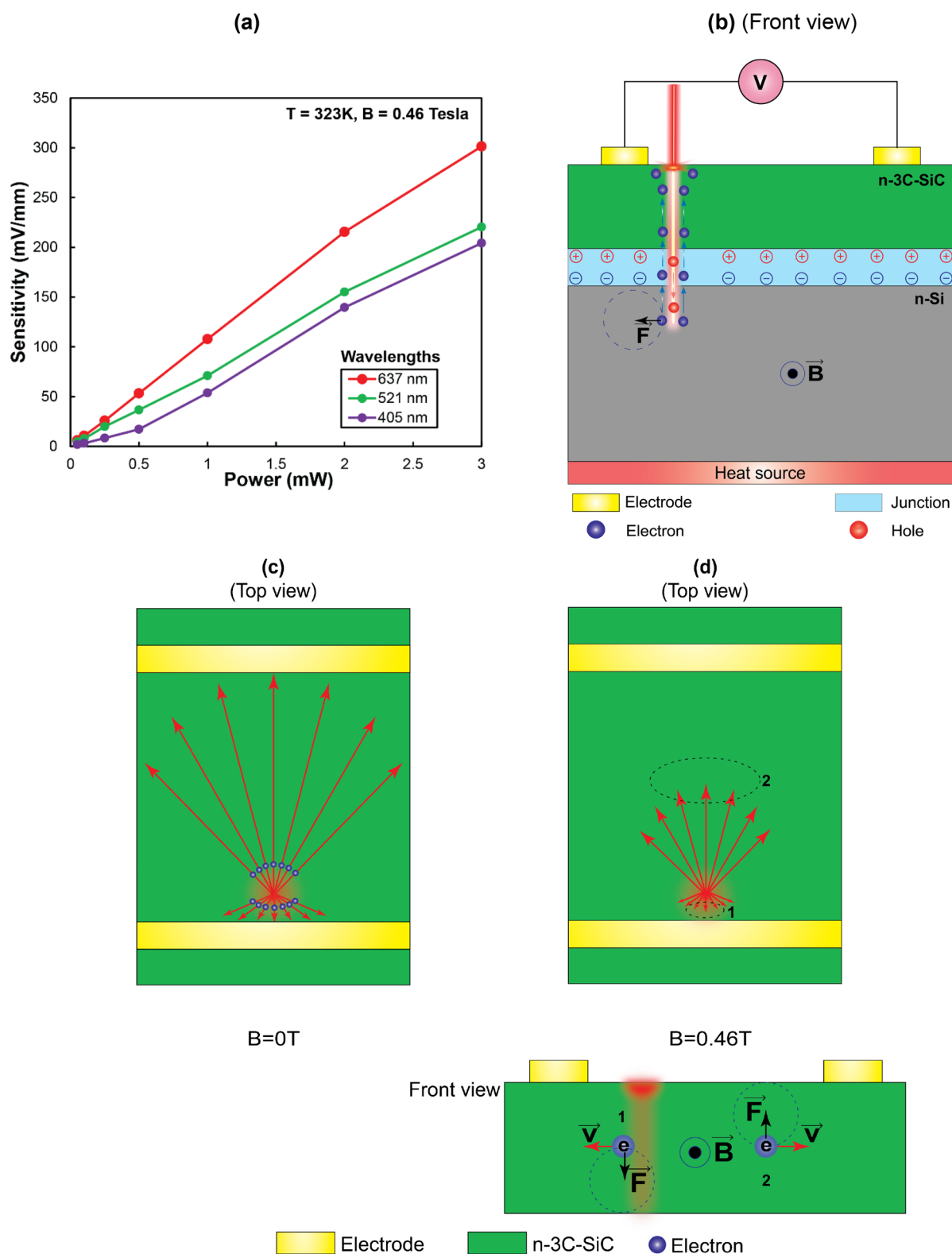


Figure 7. Impact of opto-thermo-magnetic effects on the n-3C-SiC/n-Si heterojunction in case 2. (a) Sensitivity–power relationship of devices at three wavelengths with thermo-magnetic impacts (temperature is 323 K, and magnetic field is 0.46 T). (b) Carrier distribution mechanism under opto-thermo-magneto impacts. (c) The diffusion current distribution in the n-3C-SiC layer without magnetic field and the direction of movement of electrons. (d) The diffusion current distribution in the n-3C-SiC layer with magnetic field and the direction of movement of electrons.

electrons move upward toward the SiC layer in the direction of the Oz axis because of the built-in electric field at the heterojunction, so the Lorentz force has no effect on the electrons in this layer (magnetic field \vec{B} is

parallel to the direction of movement of the electrons). In this case, thermal energy still plays a dominant role in the generation of e–h pairs. When the electrons reach the 3C-SiC layer and tend to move or diffuse laterally

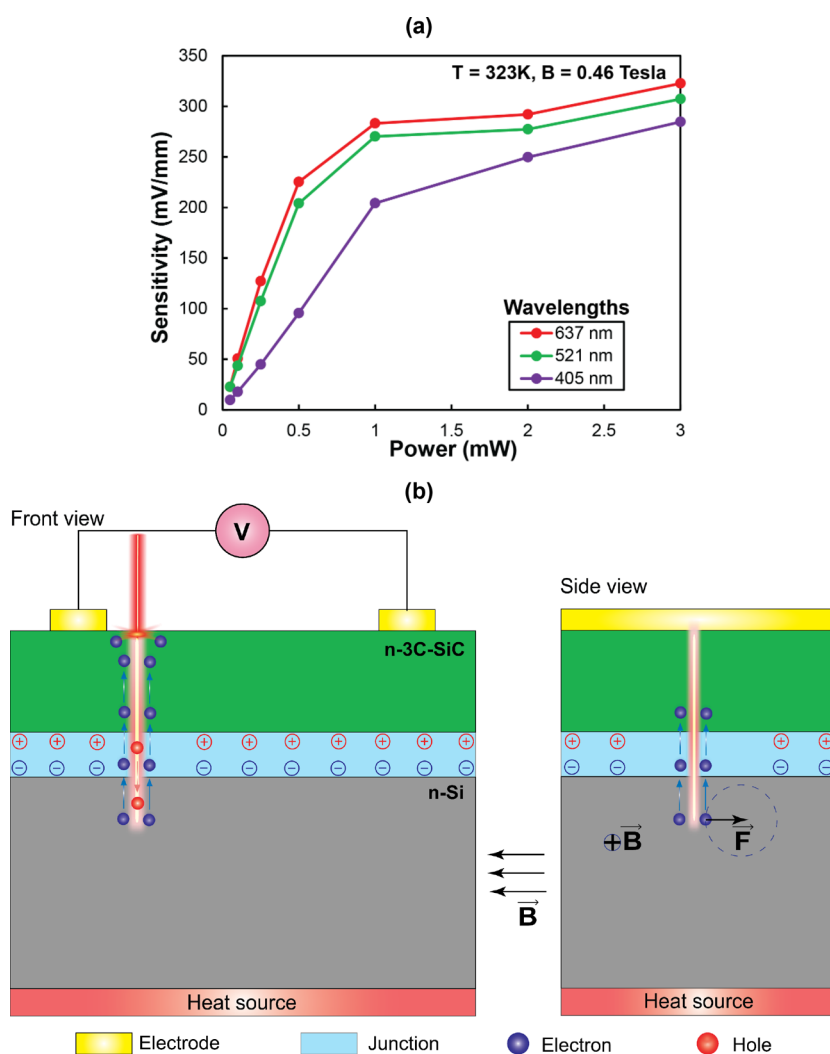


Figure 8. Impact of opto-thermo-magnetic effects on the n-3C-SiC/n-Si heterojunction in case 3. (a) Sensitivity–power relationship of devices at three wavelengths with thermo-magneto impacts (temperature is 323 K, and magnetic field is 0.46 T). (b) Carrier distribution mechanism with thermo-magneto effects under illumination conditions.

toward the other electrode, they experience significant influence from the Lorentz force. Figure 6c,d shows the diffusion current behavior within the 3C-SiC layer both in the absence and in the presence of a magnetic field. When the magnetic field is zero ($B = 0\text{ T}$), the electrons have a tendency to diffuse in all directions. If the laser light is in proximity to any electrode, that particular electrode will accumulate a substantial number of electrons, resulting in the above-mentioned result, as illustrated in Figure 4d. However, when subjected to a sufficiently strong magnetic field, electrons will additionally experience the influence of the Lorentz force. They will exhibit circular motion around a specific center, characterized by a rotational radius $r = mv/(|q|B)$ (where m is the mass of the electron, v is the velocity of the electron, q is the charge of the electron, and B is the magnetic field). Here, the Lorentz force acts as the centripetal force governing this circular motion. When the magnetic field B increases, the radius r shrinks, and the electrons orbit about that center. The diffusion current distributions in this case are circular orbitals,⁶⁵ and the electrons continue to migrate nearer to and accumulate around the electrode situated in

proximity to the light source. Nevertheless, it is important to mention that the quantity of electrons in this electrode is reduced in comparison to the situation without a magnetic field. This reduction results from the electrons undergoing circular motion under the influence of a constant magnetic field. It is worth noting that each electron travels at a distinct velocity when influenced by light, which, in turn, results in varying rotation radii for each electron within the magnetic field. Meanwhile, other electrons tend to migrate toward the electrode situated at a greater distance, following a circular orbit, which leads to a reduction in the electron concentration at that particular electrode. In short, the presence of the magnetic field extends the diffusion path of electrons, resulting in a decrease in electron concentration at both electrodes. This leads to a sharp drop in LPE as well as sensitivity.

When the direction of magnetic field vector \vec{B} is reversed (i.e., aligned with the same direction as the Oz axis), the result remains consistent.

2. Case 2

In case 2, all experimental parameters are identical to those in case 1, except for the direction of the magnetic

field. In this instance, magnetic field vector \vec{B} aligns with the same direction as the Oy axis. The results pertaining to LPE and sensitivity closely resemble the findings from case 1, as shown in Figure 7a. However, it is essential to emphasize that the movement of electrons in both layers will be different from that in case 1. The electrons within the Si layer move upward under the opto-thermo effects. These electrons experience the effects of the Lorentz force and revolve around a point in the presence of a constant magnetic field (0.46 T). However, even in the presence of this circular motion, the combined effects of light and heat remain sufficiently influential to push the majority of these electrons to move upward the 3C-SiC layer, as depicted in Figure 7b. Here, when no magnetic field exists, the analysis aligns with that of case 1, as shown in Figure 7c. Under the influence of a constant magnetic field, electrons moving in the direction of region 1 exhibit a circular motion around a point, with the Lorentz force acting in a downward direction toward the bottom surface of the 3C-SiC layer, as illustrated in Figure 7d. Conversely, electrons moving in the direction of region 2 display the opposite behavior. This distribution of electrons leads to an accumulation of electrons on both the upper and lower surfaces of the 3C-SiC layer, causing a reduction in the number of electrons moving toward the two electrodes. Naturally, the electrode in close proximity to the light source will continue to receive a greater number of electrons in comparison to the electrode situated farther away from the light.

3. Case 3

In this case setup, the magnetic field B parallels the Ox direction. The results obtained in the third case align with those obtained in the case of opto-thermal impacts in the absence of a magnetic field, as illustrated in Figure 8a. In the Si substrate, the electrons undergo rotational motion around a central point and are operated upon by the Lorentz force, as shown in Figure 8b. This rationale corresponds to that in case 2. When electrons are in the 3C-SiC layer, the Lorentz force is no longer active (the main diffusion is parallel to the magnetic field). Therefore, the results obtained from the thermo-magneto-optoelectronic characteristic remain consistent with those derived from the thermo-optoelectronic characteristic.

In addition, the performance of the PSD using the n-3C-SiC/n-Si heterostructure is compared to that of other Si-based structures, as presented in Table S2.

4. CONCLUSIONS

The optoelectronic and self-powered characteristics of an n-3C-SiC/n-Si heterostructure subjected to various thermal and magnetic conditions were experimentally studied in this work. The effects of electrode distances, laser wavelengths, and laser powers on the LPE and PSDs were thoroughly investigated. In addition, the sensitivity of PSDs under complex opto-thermo-magnetic environments was also analyzed and explained according to the generation and transportation mechanisms of e-h pairs in the n-3C-SiC/n-Si heterostructure. The results demonstrate a substantial influence of the thermo-magnetic environment on the sensitivity of the PSD sensor. This paper can serve as a valuable reference for applications of sensors in

harsh environments. The potential for using these combined effects to increase the sensitivity remains an interesting topic for further research.

■ ASSOCIATED CONTENT

Data Availability Statement

The data that support the plots within this paper and the other findings of this study are available from the corresponding author upon reasonable request.

Supporting Information

The Supporting Information is available free of charge at <https://pubs.acs.org/doi/10.1021/acs.jpcc.3c06149>.

Fabrication process of the n-3C-SiC/n-Si heterostructure devices; experimental setup for characterization of the optoelectronic effect in the n-3C-SiC/n-Si heterostructure under a thermo-magnetic environment; experimental instruments and setup; effects of electrode spacings and wavelength on the photovoltage at room temperature and without a magnetic field; the response and recovery time of the n-3C-SiC/n-Si heterostructure under the laser illumination at $76.2 \mu\text{m}$ from the central position between the two electrodes; and performance parameters of Si-based position sensitive detectors (PDF)

■ AUTHOR INFORMATION

Corresponding Authors

Dinh Gia Ninh – School of Engineering and Built Environment, Griffith University, Gold Coast, QLD 4215, Australia; Group of Materials and Structures, School of Mechanical Engineering, Hanoi University of Science and Technology, Hanoi 100000, Vietnam; orcid.org/0000-0002-9903-8847; Email: ninh.dinh@griffithuni.edu.au, ninh.dinhgia@hust.edu.vn

Dzung Viet Dao – Queensland Micro and Nanotechnology Centre (QMNC), Griffith University, Brisbane, QLD 4111, Australia; School of Engineering and Built Environment, Griffith University, Gold Coast, QLD 4215, Australia; orcid.org/0000-0002-6348-0879; Email: d.dao@griffith.edu.au

Authors

Tuan-Hung Nguyen – Queensland Micro and Nanotechnology Centre (QMNC), Griffith University, Brisbane, QLD 4111, Australia; School of Engineering and Built Environment, Griffith University, Gold Coast, QLD 4215, Australia

Cong Thanh Nguyen – Queensland Micro and Nanotechnology Centre (QMNC), Griffith University, Brisbane, QLD 4111, Australia; orcid.org/0000-0001-6461-8529

Nguyen Vu Thu Hien – Group of Materials and Structures, School of Mechanical Engineering, Hanoi University of Science and Technology, Hanoi 100000, Vietnam

Dang D.H. Tran – Queensland Micro and Nanotechnology Centre (QMNC), Griffith University, Brisbane, QLD 4111, Australia; School of Engineering and Built Environment, Griffith University, Gold Coast, QLD 4215, Australia; orcid.org/0000-0003-0829-8406

Pablo Guzman – Queensland Micro and Nanotechnology Centre (QMNC), Griffith University, Brisbane, QLD 4111,

- Australia; School of Engineering and Built Environment, Griffith University, Gold Coast, QLD 4215, Australia
- Braiden Tong** – Queensland Micro and Nanotechnology Centre (QMNC), Griffith University, Brisbane, QLD 4111, Australia; School of Engineering and Built Environment, Griffith University, Gold Coast, QLD 4215, Australia; orcid.org/0000-0002-7548-2521
- Hong-Quan Nguyen** – Queensland Micro and Nanotechnology Centre (QMNC), Griffith University, Brisbane, QLD 4111, Australia
- Emily Lakis** – Queensland Micro and Nanotechnology Centre (QMNC), Griffith University, Brisbane, QLD 4111, Australia; School of Engineering and Built Environment, Griffith University, Gold Coast, QLD 4215, Australia
- Trung-Hieu Vu** – Queensland Micro and Nanotechnology Centre (QMNC), Griffith University, Brisbane, QLD 4111, Australia; School of Engineering and Built Environment, Griffith University, Gold Coast, QLD 4215, Australia; orcid.org/0000-0003-4431-1874
- Erik W. Streed** – Institute for Glycomics, Griffith University, Southport 4222, Australia
- Yong Zhu** – School of Engineering and Built Environment, Griffith University, Gold Coast, QLD 4215, Australia
- Tuan-Khoa Nguyen** – Queensland Micro and Nanotechnology Centre (QMNC), Griffith University, Brisbane, QLD 4111, Australia; orcid.org/0000-0003-1271-9576
- Van Thanh Dau** – School of Engineering and Built Environment, Griffith University, Gold Coast, QLD 4215, Australia
- Nam-Trung Nguyen** – Queensland Micro and Nanotechnology Centre (QMNC), Griffith University, Brisbane, QLD 4111, Australia

Complete contact information is available at:
<https://pubs.acs.org/10.1021/acs.jpcc.3c06149>

Author Contributions

Dinh Gia Ninh: Conceptualization, Investigation, Methodology, Data curation, Formal analysis, Writing – original draft. Tuan-Hung Nguyen: Investigation, Formal analysis, Writing – original draft. Cong Thanh Nguyen: Investigation, Formal analysis, Writing – original draft. Nguyen Vu Thu Hien: Investigation, Formal analysis. Dang D.H. Tran: Data curation. Pablo Guzman: Investigation. Braiden Tong: Formal analysis, Writing – review and editing. Hong-Quan Nguyen: Fabrication. Emily Lakis: Data curation. Trung-Hieu Vu: Data curation. Erik W. Streed: Formal analysis, Facilities and technical equipment. Yong Zhu: Conceptualization, Supervision, Writing – review and editing. Tuan-Khoa Nguyen: Fabrication, Data curation. Van Thanh Dau: Supervision, Writing – review and editing, Project administration. Nam-Trung Nguyen: Project administration, Writing – review and editing, Funding acquisition. Dzung Viet Dao: Conceptualization, Project administration, Supervision, Writing – review and editing, Funding acquisition. All authors read and commented on the paper.

Notes

The authors declare no competing financial interest. This article does not contain any studies with human participants or animals performed by any of the authors. There are no individual participants included in the study.

ACKNOWLEDGMENTS

This work used the Queensland node of the NCRIS-enabled Australian National Fabrication Facility (ANFF) and was supported by the Australian Research Council under a Discovery project (DP220101252). Laser measurements were performed at the Biophysics Laser Lab, Institute for Glycomics, Griffith University. The SAED and TEM images were taken by the Center for Microscopy and Microanalysis, The University of Queensland, Brisbane, QLD, Australia, 4072. The authors are grateful for the support of research centers and funds.

REFERENCES

- (1) Taniguchi, M.; Takei, H.; Tomiyasu, K.; Sakamoto, O.; Naono, N. Sensing The Performance of Artificially Intelligent Nanopores Developed by Integrating Solid-State Nanopores with Machine Learning Methods. *J. Phys. Chem. C* **2022**, *126*, 12197–12209.
- (2) Gong, Y.; Zhang, Y. Z.; Fang, S.; Liu, C.; Niu, J.; Li, G.; Li, F.; Li, X.; Cheng, T.; Lai, W. Y. Artificial Intelligent Optoelectronic Skin with Anisotropic Electrical and Optical Responses for Multi-Dimensional Sensing. *Appl. Phys. Rev.* **2022**, *9*, 021403–021403.
- (3) Huang, Y. C.; Liu, Y.; Ma, C.; Cheng, H. C.; He, Q.; Wu, H.; Wang, C.; Lin, C. Y.; Huang, Y.; Duan, X. Sensitive Pressure Sensors Based on Conductive Microstructured Air-Gap Gates and Two-Dimensional Semiconductor Transistors. *Nat. Electron.* **2020**, *3*, 59–69.
- (4) Haick, H.; Tang, N. Artificial Intelligence in Medical Sensors for Clinical Decisions. *ACS Nano* **2021**, *15*, 3557–3567.
- (5) Fatema, A.; Poondla, S.; Mishra, R.; Hussain, A. M. A Low-Cost Pressure Sensor Matrix for Activity Monitoring in Stroke Patients Using Artificial Intelligence. *IEEE Sens. J.* **2021**, *21*, 9546–9552.
- (6) Lou, Z.; Wang, L.; Shen, G. Recent Advances in Smart Wearable Sensing Systems. *Adv. Mater. Technol.* **2018**, *3*, No. 1800444.
- (7) Kumar, A. Methods and Materials for Smart Manufacturing: Additive Manufacturing, Internet of Things, Flexible Sensors and Soft Robotics. *Manuf. Lett.* **2018**, *15*, 122–125.
- (8) Yao, G.; Xu, L.; Cheng, X.; Li, Y.; Huang, X.; Guo, W.; Liu, S.; Wang, Z. L.; Wu, H. Bioinspired Triboelectric Nanogenerators as Self-Powered Electronic Skin for Robotic Tactile Sensing. *Adv. Funct. Mater.* **2019**, *30*, No. 1907312.
- (9) Liu, J.; Guo, Z.; Meng, F.; Jia, Y.; Liu, J. A Novel Antimony–Carbon Nanotube–Tin Oxide Thin Film: Carbon Nanotubes as Growth Guider and Energy Buffer. Application for Indoor Air Pollutants Gas Sensor. *J. Phys. Chem. C* **2008**, *112*, 6119–6125.
- (10) Boutry, C. M.; Negre, M.; Jorda, M.; Vardoulis, O.; Chortos, A.; Khatib, O.; Bao, Z. A Hierarchically Patterned, Bioinspired E-Skin Able to Detect the Direction of Applied Pressure for Robotics. *Sci. Robot.* **2018**, *3*, No. eaau6914.
- (11) Münzer, A. M.; Seo, W.; Morgan, G. J.; Michael, Z. P.; Zhao, Y.; Melzer, K.; Scarpa, G.; Star, A. Sensing Reversible Protein–Ligand Interactions with Single-Walled Carbon Nanotube Field-Effect Transistors. *J. Phys. Chem. C* **2014**, *118*, 17193–17199.
- (12) Rezapour, M. R.; Myung, C. W.; Yun, J.; Ghassami, A.; Li, N.; Yu, S. U.; Hajjibabaei, A.; Park, Y.; Kim, K. S. Graphene and Graphene Analogs toward Optical, Electronic, Spintronic, Green-Chemical, Energy-Material, Sensing, and Medical Applications. *ACS Appl. Mater. Interfaces* **2017**, *9*, 24393–24406.
- (13) Nambiar, S.; Yeow, J. T. W. Conductive Polymer-Based Sensors for Biomedical Applications. *Biosens. Bioelectron.* **2011**, *26*, 1825–1832.
- (14) Liu, Y.; Pharr, M.; Salvatore, G. A. Lab-On-Skin: A Review of Flexible and Stretchable Electronics for Wearable Health Monitoring. *ACS Nano* **2017**, *11*, 9614–9635.
- (15) Schwartz, G.; Tee, B. C. K.; Mei, J.; Appleton, A. L.; Kim, D. H.; Wang, H.; Bao, Z. Flexible Polymer Transistors with High Pressure Sensitivity for Application in Electronic Skin and Health Monitoring. *Nat. Commun.* **2013**, *4*, 1859.

- (16) Wang, X.; Li, Z.; Xu, W.; Kulkarni, S.; Batabyal, S. K.; Zhang, S.; Cao, A.; Wong, L. H. TiO₂ Nanotube Arrays Based Flexible Perovskite Solar Cells with Transparent Carbon Nanotube Electrode. *Nano Energy* **2015**, *11*, 728–735.
- (17) Liu, K.; Sakurai, M.; Liao, M.; Aono, M. Giant Improvement of the Performance of ZnO Nanowire Photodetectors by Au Nanoparticles. *J. Phys. Chem. C* **2010**, *114*, 19835–19839.
- (18) Tian, W.; Wang, Y.; Chen, L.; Li, L. Self-Powered Nanoscale Photodetectors. *Small* **2017**, *13*, No. 1701848.
- (19) Zou, J.-P.; Zhang, Q.; Huang, K.; Marzari, N. Ultraviolet Photodetectors Based on Anodic TiO₂ Nanotube Arrays. *J. Phys. Chem. C* **2010**, *114*, 10725–10729.
- (20) Huang, Y. C.; Parimi, V.; Chang, W. C.; Syu, H. J.; Su, Z. C.; Lin, C. F. Silicon-Based Photodetector for Infrared Telecommunication Applications. *IEEE Photon. J.* **2021**, *13*, 1–7.
- (21) Sarkar, S.; Makhal, A.; Lakshman, K.; Bora, T.; Dutta, J.; Kumar Pal, S. Dual-Sensitization via Electron and Energy Harvesting in CdTe Quantum Dots Decorated ZnO Nanorod-Based Dye-Sensitized Solar Cells. *J. Phys. Chem. C* **2012**, *116*, 14248–14256.
- (22) Gao, L.; Lu, S.; Xie, W.; Chen, X.; Wu, L.; Wang, T.; Wang, A.; Yue, C.; Tong, D.; Lei, W.; et al. A Self-Powered and Self-Functional Tracking System Based on Triboelectric-Electromagnetic Hybridized Blue Energy Harvesting Module. *Nano Energy* **2020**, *72*, No. 104684.
- (23) Sudevalayam, S.; Kulkarni, P. Energy Harvesting Sensor Nodes: Survey and Implications. *IEEE Communications Surveys Tutorials* **2011**, *13*, 443–461.
- (24) Peng, L.; Hu, L.; Fang, X. Energy Harvesting for Nanostructured Self-Powered Photodetectors. *Adv. Funct. Mater.* **2014**, *24*, 2591–2610.
- (25) Moon, I. K.; Ki, B.; Yoon, S.; Choi, J.; Oh, J. Lateral Photovoltaic Effect in Flexible Free-Standing Reduced Graphene Oxide Film for Self-Powered Position-Sensitive Detection. *Sci. Rep.* **2016**, *6*, 33525.
- (26) Nguyen, T. H.; Nguyen, T.; Faisal, A. R. M.; Pham, T. A.; Dinh, T.; Nguyen, H. Q.; Streed, E. W.; Vu, T. H.; Fastier-Wooler, J.; Duran, P. G.; Dau, V. T.; Nguyen, N. T.; Dao, D. V.; et al. Ultrasensitive Self-Powered Position-Sensitive Detector Based on N-3C-SiC/P-Si Heterojunctions. *ACS Appl. Electron. Mater.* **2022**, *4*, 768–775.
- (27) Javadi, M. S.; Gholami, M.; Abdi, Y. IR Position-Sensitive Detectors Based on Double-Junction Asymmetric TiO₂/MoS₂/Reduced Graphene-Oxide Sandwiches. *J. Mater. Chem. C* **2018**, *6*, 8444–8452.
- (28) Faisal, A. R. M.; Qamar, A.; Nguyen, T.; Dinh, T.; Phan, H. P.; Nguyen, H.; Duran, P. G.; Streed, E. W.; Dao, D. V. Ultra-Sensitive Self-Powered Position-Sensitive Detector Based on Horizontally-Aligned Double 3C-SiC/Si Heterostructures. *Nano Energy* **2021**, *79*, No. 105494.
- (29) Saive, R. S-Shaped Current–Voltage Characteristics in Solar Cells: A Review. *IEEE Journal of Photovoltaics* **2019**, *9*, 1477–1484.
- (30) Salim, T.; Sun, S.; Abe, Y.; Krishna, A.; Grimsdale, A. C.; Lam, Y. M. Perovskite-Based Solar Cells: Impact of Morphology and Device Architecture on Device Performance. *J. Mater. Chem. A* **2015**, *3*, 8943–8969.
- (31) Li, C.; Han, C.; Zhang, Y.; Zang, Z.; Wang, M.; Tang, X.; Du, J. Enhanced Photoresponse of Self-Powered Perovskite Photodetector Based on ZnO Nanoparticles Decorated CsPbBr₃ Films. *Solar Energy Mater. Solar Cells* **2017**, *172*, 341–346.
- (32) Borges-Martínez, M.; Álvarez, D.; Montenegro-Pohlhammer, N.; Menéndez, M.; Lopez, R.; Cárdenas-Jirón, G. I. Assessment of BODIPY–Oxasmaragdyrin Dyads for Dye-Sensitized Solar Cells: Aromaticity, Photosensitization Capability, and Charge Transport. *J. Phys. Chem. C* **2019**, *123*, 19362–19375.
- (33) Ma, J.; Chen, M.; Qiao, S.; Chang, J.; Fu, G.; Wang, S. Photovoltaic–Pyroelectric Coupled Effect in Ag₂Se/Si Heterojunction for Broad-Band, Ultrafast, Self-Powered, Position-Sensitive Detectors. *ACS Photonics* **2022**, *9*, 2160–2169.
- (34) Cao, Y.; Zhao, Z.; Bao, P.; Gan, Z.; Wang, H. Lateral Photovoltaic Effect in Silk-Protein-Based Nanocomposite Structure for Physically Transient Position-Sensitive Detectors. *Phys. Rev. Appl.* **2021**, *15*, No. 054011.
- (35) Cong, R.; Qiao, S.; Liu, J.; Mi, J.; Yu, W.; Liang, B.; Fu, G.; Pan, C.; Wang, S. Ultrahigh, Ultrafast, and Self-Powered Visible-Near-Infrared Optical Position-Sensitive Detector Based on a CVD-Prepared Vertically Standing Few-Layer MoS₂/Si Heterojunction. *Adv. Sci.* **2017**, *5*, No. 1700502.
- (36) Wang, X.; Song, B.; Huo, M.; Song, Y.; Lv, Z.; Zhang, Y.; Wang, Y.; Song, Y.; Wen, J.; Sui, Y.; et al. Fast and Sensitive Lateral Photovoltaic Effects in Fe₃O₄/Si Schottky Junction. *RSC Adv.* **2015**, *5*, 65048–65051.
- (37) Du, X.; Tian, W.; Zhang, Z.; Hui, B.; Pan, J.; Sun, J.; Zhang, K. Defect Promoted Photothermoelectric Effect in Densely Aligned ZnO Nanorod Arrays for Self-Powered Position-Sensitive Photodetection. *Journal of Materiomics* **2022**, *8*, 693–701.
- (38) Javadi, M.; Gholami, M.; Torbatiyan, H.; Abdi, Y. Hybrid Organic/Inorganic Position-Sensitive Detectors Based on PEDOT:PSS/N-Si. *Appl. Phys. Lett.* **2018**, *112*, No. 113302.
- (39) Wang, W. H.; Du, R. X.; Guo, X. T.; Jiang, J.; Zhao, W. W.; Ni, Z. H.; Wang, X. R.; You, Y. M.; Ni, Z. H. Interfacial Amplification for Graphene-Based Position-Sensitive-Detectors. *Light: Sci. Appl.* **2017**, *6*, e17113–e17113.
- (40) Zhang, C.; Zhu, C.; Yang, Z.; Lin, D.; Wu, C.; Chen, S.; Yang, Y.; Wang, L.; Zhou, Y.; Luo, L. Fabrication of a Periodic Inverse Micropyramid (PIMP)-Si/in₂Se₃ Heterojunction Photodetector Array for RGB-IR Image Sensing Application. *Adv. Mater. Technol.* **2022**, *8*, No. 2200863.
- (41) Chu, Y. L.; Liu, Y. H.; Chu, T. T.; Young, S. J. Improved UV-Sensing of Au-Decorated ZnO Nanostructure MSM Photodetectors. *IEEE Sens. J.* **2022**, *22*, 5644–5650.
- (42) Huang, X.; Mei, C.; Gan, Z.; Zhou, P.; Wang, H. Lateral Photovoltaic Effect in P-Type Silicon Induced by Surface States. *Appl. Phys. Lett.* **2017**, *110*, No. 121103.
- (43) Dong, X.; Zheng, D.; Lu, J.; Niu, Y.; Wang, H. Selectively Enhanced Violet and Infrared Position Sensitive Photodetectors Based on RTA Treated ZnO/Si. *Appl. Surf. Sci.* **2021**, *566*, 150687–150687.
- (44) Hao, L.; Xu, H.; Dong, S.; Du, Y.; Luo, L.; Zhang, C.; Liu, H.; Wu, Y.; Liu, Y. SnSe/SiO₂/Si Heterostructures for Ultrahigh-Sensitivity and Broadband Optical Position Sensitive Detectors. *IEEE Electron Device Lett.* **2019**, *40*, 55–58.
- (45) Ashar, A. Z.; Ganesh, N.; Narayan, K. S. Hybrid Perovskite-Based Position-Sensitive Detectors. *Adv. Electron. Mater.* **2017**, *4*, No. 1700362.
- (46) Ganesh, N.; Schutt, K.; Nayak, P. K.; Snaith, H. J.; Narayan, K. S. 2D Position-Sensitive Hybrid-Perovskite Detectors. *ACS Appl. Mater. Interfaces* **2021**, *13*, 54527–54535.
- (47) Qiao, S.; Feng, K.; Li, Z.; Fu, G.; Wang, S. Ultrahigh, Ultrafast and Large Response Size Visible-Near-Infrared Optical Position Sensitive Detectors Based on CIGS Structures. *J. Mater. Chem. C* **2017**, *5*, 4915–4922.
- (48) Zhu, H.; Shan, C. X.; Wang, L. K.; Zheng, J.; Zhang, J. Y.; Yao, B.; Shen, D. Z. Metal–Oxide–Semiconductor-Structured MgZnO Ultraviolet Photodetector with High Internal Gain. *J. Phys. Chem. C* **2010**, *114*, 7169–7172.
- (49) DuttaGupta, S.; Itoh, R.; Fukami, S.; Ohno, H. Angle Dependent Magnetoresistance in Heterostructures with Antiferromagnetic and Non-Magnetic Metals. *Appl. Phys. Lett.* **2018**, *113*, No. 202404.
- (50) Brinkman, A.; Huijben, M.; van Zalk, M.; Huijben, J.; Zeitler, U.; Maan, J. C.; van der Wiel, W. G.; Rijnders, G.; Blank, D. H. A.; Hilgenkamp, H. Magnetic Effects at the Interface between Non-Magnetic Oxides. *Nat. Mater.* **2007**, *6*, 493–496.
- (51) Hu, B.; Wu, Y. Tuning Magnetoresistance between Positive and Negative Values in Organic Semiconductors. *Nat. Mater.* **2007**, *6*, 985–991.
- (52) Bloom, F. L.; Wagemans, W.; Kemerink, M.; Koopmans, B. Separating Positive and Negative Magnetoresistance in Organic Semiconductor Devices. *Phys. Rev. Lett.* **2007**, *99*, No. 257201.

- (53) Mehregany, M.; Zorman, C. A. SiC MEMS: Opportunities and Challenges for Applications in Harsh Environments. *Thin Solid Films* **1999**, 355–356, 518–524.
- (54) Hussain, T.; Farokh Niaei, A. H.; Searles, D. J.; Hankel, M. Three-Dimensional Silicon Carbide from Siligraphene as a High Capacity Lithium Ion Battery Anode Material. *J. Phys. Chem. C* **2019**, 123, 27295–27304.
- (55) Mehregany, M.; Zorman, C. A.; Rajan, N.; Wu, C. H. Silicon Carbide MEMS for Harsh Environments. *Proc. IEEE* **1998**, 86, 1594–1609.
- (56) Tanner, P.; Iacopi, A.; Phan, H. P.; Dimitrijević, S.; Hold, L.; Chaik, K.; Walker, G.; Dao, D. V.; Nguyen, N. T. Excellent Rectifying Properties of the N-3C-SiC/p-Si Heterojunction Subjected to High Temperature Annealing for Electronics, MEMS, and LED Applications. *Sci. Rep.* **2017**, 7, 17734.
- (57) Senesky, D. G.; Jamshidi, B.; Cheng, K. B.; Pisano, A. P. Harsh Environment Silicon Carbide Sensors for Health and Performance Monitoring of Aerospace Systems: A Review. *IEEE Sens. J.* **2009**, 9, 1472–1478.
- (58) Baltes, H. P.; Popovic, R. S. Integrated Semiconductor Magnetic Field Sensors. *Proc. IEEE* **1986**, 74, 1107–1132.
- (59) Pankove, J. I.; Dover Publications. *Optical Processes in Semiconductors*; Dover Publications, Inc: New York, 2018.
- (60) Yu, C. Q.; Wang, H. Large Near-Infrared Lateral Photovoltaic Effect Observed in Co/Si Metal-Semiconductor Structures. *App. Phys. Lett.* **2010**, 96, No. 171102.
- (61) Yu, C.; Wang, H.; Xiao, S.; Xia, Y. Direct Observation of Lateral Photovoltaic Effect in Nano-Metal-Films. *Opt. Express* **2009**, 17, 21712–21712.
- (62) Zhang, Y.; Zhang, Y.; Yao, T.; Hu, C.; Sui, Y.; Wang, X. Ultrahigh Position Sensitivity and Fast Optical Relaxation Time of Lateral Photovoltaic Effect in Sb₂Se₃/P-Si Junctions. *Opt. Express* **2018**, 26, 34214–34223.
- (63) Sze, S. M.; Li, Y.; Ng, K. K. *Physics of Semiconductor Devices*; John Wiley & Sons, 2021.
- (64) Nguyen, T.; Dinh, T.; Bell, J.; Dau, V. T.; Nguyen, N.; Dao, D. V. Light-Harvesting Self-Powered Monolithic-Structure Temperature Sensing Based on 3C-SiC/Si Heterostructure. *ACS Appl. Mater. Interfaces* **2022**, 14, 22593–22600.
- (65) Zhou, P.; Gan, Z.; Huang, X.; Mei, C.; Xia, Y.; Wang, H. Size-Dependent Magnetic Tuning of Lateral Photovoltaic Effect in Nonmagnetic Si-Based Schottky Junctions. *Sci. Rep.* **2017**, 7, 46377.